

# Accurate Parameters of the Mass Distribution in Spiral Galaxies:

## 1. Fabry–Perot Observations of NGC 5585

Sébastien Blais–Ouellette

Département de physique and Observatoire du mont Mégantic, Université de Montréal,  
 C.P. 6128, Succ. centre ville, Montréal, Québec, Canada. H3C 3J7 and  
 IGRAP, Observatoire de Marseille, 2 Place Le Verrier, F–13248 Marseille Cedex 04, France  
 e–mail: blaisous@astro.umontreal.ca

Claude Carignan<sup>1</sup>

Département de physique and Observatoire du mont Mégantic, Université de Montréal,  
 C.P. 6128, Succ. centre ville, Montréal, Québec, Canada. H3C 3J7  
 e–mail: carignan@astro.umontreal.ca

Philippe Amram

IGRAP, Observatoire de Marseille, 2 Place Le Verrier, F–13248 Marseille Cedex 04, France  
 e–mail: amram@observatoire.cnrs-mrs.fr

Stéphanie Côté<sup>1</sup>

Dominion Astrophysical Observatory, Herzberg Institute of Astrophysics, National  
 Research Council of Canada, 5071 West Saanich Rd., Victoria, BC, Canada. V8X 4M6  
 e–mail: Stephanie.Cote@hia.nrc.ca

## ABSTRACT

Using the example of the Sd galaxy NGC 5585, it is shown that high resolution 2–D H II kinematical data are necessary to determine accurately the parameters of the mass (luminous & dark) distribution in spirals. New CFHT Fabry–Perot H $\alpha$  observations are combined with low resolution (20 ‐) Westerbork H I data to study its mass distribution. Using the combined rotation curve and best fit models, it can be seen that  $(\mathcal{M}/L_B)_*$  of the luminous disk goes from 0.3 using only the H I rotation curve, to 0.8 using both the optical and the radio data. This reduces the dark–to–luminous mass ratio in NGC 5585 by  $\sim 30\%$  through increasing the dark matter halo core radius by nearly the same amount. This shows the importance of the inner, rising part of the

---

<sup>1</sup>Visiting Astronomers, Canada–France–Hawaii Telescope, operated by the National Research Council of Canada, the Centre National de la Recherche Scientifique de France, and the University of Hawaii.

rotation curve for the accurate determination of the parameters of the global mass (luminous & dark) distribution and suggests that such a fine tuning of the rotation velocities using high resolution 2-D H II kinematics is necessary to look at correlations between the parameters of the dark matter component and other properties of galaxies.

*Subject headings:* cosmology: dark matter — galaxies: individual (NGC 5585, NGC 3198)  
— galaxies: fundamental parameters (masses) — techniques: interferometric

## 1. INTRODUCTION

In the last 25 years, a large number of rotation curves were derived for spiral (Sp) and dwarf irregular (dIrr) galaxies from 2-D H I kinematics obtained with synthesis instruments such as the Westerbork (WSRT) array, the Very Large Array (VLA), and the Australia Telescope (AT) (for a good review of the first 20 years, see e.g. Ashman 1992). In many galaxies, especially late-type spirals and dwarf irregulars, the H I extends much further out than the optical and thus than the H II emission. An argument often used is that, since the H I rotation curve probes the gravitational potential in the dark matter dominated region, it is best suited to derive the parameters of the mass distribution and especially of the dark matter halo. However, as will be shown, the parameters of the mass models (and especially of the dark matter distribution) are very sensitive not only to the flat part of the rotation curve (best probed by the H I observations) but also to the rising inner part, which can be derived with greater precision using 2-D H $\alpha$  observations (see e.g. Amram et al. 1992, 1994, 1995, 1996). This is also well illustrated by Swaters (1999) who clearly shows the impact of varying the position of the first few velocity points (within the uncertainties due to beam smearing) on the parameters of the mass models even in the dark matter dominated dwarfs.

What is now regarded as the classical method to study the mass distribution (van Albada et al. 1985, Carignan & Freeman 1985) is illustrated in Fig.1a, which shows the analysis of the mass distribution of NGC 5585 using its H I rotation curve (Côté, Carignan, & Sancisi 1991). See also Begeman 1987, Broeils 1992 and Côté 1995 for many more examples. First, the rotation curve is obtained by fitting a “tilted-ring” model to the H I velocity field in order to represent the warp of the H I disk, which is almost always present. The accuracy of the model representation is then checked by looking at the residual (data – model) map (Warner 1973, Sancisi & Allen 1979). Then the luminosity profile in

the reddest band available to probe the mass dominant population is transformed into a mass distribution for the stellar disk, assuming a constant value of  $(\mathcal{M}/L_B)_\star$  (Casertano 1983, Carignan 1985). For the contribution of the gaseous component, the H I radial profile scaled by 1.33 is used to account for He. The difference between the observed rotation curve and the computed contribution to the curve of the luminous (stars & gas) component is thus the contribution of the dark component, which can be represented by an isothermal halo (Carignan 1985) or some other functional form (e.g. Lake & Feinswog 1989). The model of Fig.1a allows us to study the dark-to-luminous mass ratio as a function of radius, as shown in Fig.1b. Naturally, this is for standard gravity. Some alternative models, such as MOND, have also been explored (Milgrom 1983, Sanders 1996, McGaugh & de Blok 1998).

The example of NGC 5585 shows the importance of an accurate determination of the rising part of the rotation curve, since this is the part that mainly constrains the values of two of the three free parameters of the mass model; namely, the mass-to-light ratio of the luminous stellar disk  $(\mathcal{M}/L_B)_\star$  and the core radius  $r_c$ . The third parameter, the one dimensional velocity dispersion  $\sigma$  of the dark isothermal halo is mainly constrained by the outer part of the rotation curve. The H I observations, often optimized for maximum sensitivity in the outer parts, have in most of the published studies a resolution of only 20–45 " (higher resolution is naturally possible by adding longer baselines when there is sufficient H I flux). Attempts have been made to correct for the effect of “beam smearing”, which can be very important in the inner parts because of the strong velocity gradient (sometimes combined with a strong radial distribution gradient) across the large H I beam. This is examined using as an example the Sc galaxy NGC 3198.

Another point that needs to be stressed is that full 2-D H II kinematical data are necessary for this work and that 1-D long-slit spectroscopy is not sufficient. This is due to the fact that the photometric parameters (we are mainly concerned with the position angle PA and photometric center in this case) used to position the slits on the galaxies can sometime be quite different from the kinematical parameters. Naturally, if the slit is positioned with a slightly wrong PA, the velocities will necessarily be underestimated. This is well illustrated for the case of the rotation curves of galaxies in clusters (Whitmore, Forbes & Rubin 1988 for the 1-D long-slit, and Amram et al. 1996 for 2-D Fabry–Perot).

The importance of the rising part of the rotation curve on the parameters for both the luminous and dark matter distributions is illustrated by two examples in section 2. Section 3 describes the new CFHT Fabry–Perot (FP) observations and data reduction of the NGC 5585 data. The H II kinematics and the optical rotation curve are discussed in Section 4, while the mass models and the parameters of the mass distribution are given in Section 5. Finally, Section 6 gives a summary of the results and draws general conclusions from this

study.

## 2. IMPORTANCE OF THE RISING PART OF THE ROTATION CURVE ON THE PARAMETERS OF THE MASS (LUMINOUS & DARK) DISTRIBUTION

It has always been thought that the problem of “beam smearing” was important mainly in early-type spirals, where the strong gradient due to the presence of the bulge was attenuated in low resolution H I data and where it was obvious that higher resolution data were necessary to see the true kinematics resulting from the centrally concentrated luminous mass distribution. In what follows, it will be shown that, while the effect of beam smearing in late-type spirals may be less dramatic, it can nevertheless have a significant impact on the derived parameters of both the luminous and the dark mass distributions.

### 2.1. The Case of NGC 5585

To show the importance of the first few points of the rotation curve in a galaxy such as NGC 5585, a model was constructed giving no weight to the first two points of the H I curve (Fig.2a). This model mimics a difference of less than 10 “ with the real position of the first two points, a very plausible effect of the large radio beams. In this model, the  $(M/L_B)_*$  of the stellar disk goes from 0.3 (Fig.1a) to 1.0 (Fig.2a), with the result that the mass of the stellar disk goes from  $\sim 20\%$  of the gaseous disk to a comparable mass. More importantly is that the dark matter halo is less centrally concentrated with a dark-to-luminous mass ratio going from 9.5 (Fig.1b) to 6.3 (Fig.2b) at the last measured point of the rotation curve. This is a difference of more than 30% in the dark-to-luminous mass ratio for a difference of less than 10 “ in the position of the first two points of the curve. As illustrated in Fig.1b & Fig.2b, the global distribution of the dark component is also totally different. This is why we think that the ideal rotation curve to study the mass distribution in galaxies should combine the high resolution of H $\alpha$  FP observations in the inner parts to the high sensitivity of the low resolution H I observations in the outer parts.

### 2.2. The Case of NGC 3198

Begeman (1989) published a Westerbork H I rotation curve of NGC 3198, where he attempted to correct for the effect of beam-smearing. Theoretically, one should be able to

calculate this effect by convolving the rapidly dropping HI density profile and the rising rotation curve inside the width of the beam. In the inner parts, his rotation velocities are systematically larger (up to  $26 \text{ km s}^{-1}$  at  $30''$ ) than the values derived in a previous HI study by Bosma (1981). If the corrections are accurate, one would expect that there should be very little gain in using high resolution H $\alpha$  data. Fig.3 and Table 1 show the best-fit model using the beam-smearing corrected HI data. It can be seen that for  $r < 3 \text{ kpc}$  and  $r > 15 \text{ kpc}$ , the model gives a good representation of the data. However, around 4 kpc, the model velocity is larger by  $\sim 10 \text{ km s}^{-1}$  compared to the measured velocity.

A best-fit model (Fig.4) was obtained by combining Begeman's HI data with the FP H $\alpha$  kinematical data of Corradi et al. (1991). We see that while the agreement between the two sets of data appears good over all, the optical velocities are somewhat smaller in the steep rising part of the rotation curve. As can be seen in Table 1, the dark-to-luminous mass ratio at the last measured point has changed very little between the two models ( $2.9 \rightarrow 3.0$ ), but the shape of the halo has changed substantially, becoming more centrally concentrated with  $r_c$  going from 17.2 to 11.7 kpc, again a change of more than 30%. The apparently small difference in velocity ( $\sim 5 \text{ km s}^{-1}$ ) results in an increase of the dark halo central density  $\rho_0$  by nearly a factor of 2 ( $0.004 \rightarrow 0.008$ ). This suggests that Begeman (1989) may have overestimated his beam-smearing corrections.

It is instructive also to compare this result with the earlier Bosma data, which were not corrected for beam-smearing, as is the case for most HI data. NGC 3198 is an Sc galaxy, in which the velocity gradient is much smaller than in Sa or Sb galaxies and one would have thought that the effect of beam-smearing should not be that dramatic. Fig.5 shows the best fit model using that data set. We see that the mass distribution is completely different, with a much smaller disk and a dark halo that dominates completely for  $r \geq 1 \text{ kpc}$ . The result is that, with differences  $\leq 10 \text{ km s}^{-1}$  for  $0 \leq r \leq 6 \text{ kpc}$ , the dark component has nearly 10 times higher central density, which results in an increase of the dark-to-luminous mass ratio from  $\sim 1$  to  $\sim 4$ .

Many more examples could be discussed, but we think that the examples above show clearly that high resolution H $\alpha$  data are necessary to compute accurately the parameters of both the luminous and dark mass distributions.

### 3. FABRY-PEROT OBSERVATIONS & REDUCTION

Table 2 gives the optical parameters of NGC 5585 and Table 3 lists the complete observing parameters. The FP observations of the H $\alpha$  emission line were obtained in February 1994 at the Canada-France-Hawaii Telescope (CFHT). The FP etalon (CFHT1) was installed in the CFHT's Multi-Object Spectrograph (MOS). A narrow-band filter ( $\Delta\lambda = 10 \text{ \AA}$ ), centered at  $\lambda_0 = 6570 \text{ \AA}$  (nearly at the systemic velocity of NGC 5585,  $V_{sys} \approx 305 \text{ km s}^{-1}$ ), was placed in front of the etalon. The available field with no vignetting was  $\approx 8.5' \times 8.5'$ , with  $0.34'' \text{ pix}^{-1}$ . The free spectral range of  $5.66 \text{ \AA}$  ( $258 \text{ km s}^{-1}$ ) was scanned in 27 (+1 overlapping) channels, giving a sampling of  $0.2 \text{ \AA}$  ( $9.2 \text{ km s}^{-1}$ ) per channel. Eight minutes integration was spent at each channel position.

#### 3.1. Data analysis

Following normal de-biasing and flat-fielding with standard IRAF procedures, a robust 3-D cosmic-ray removal routine, that tracks cosmic rays by spatial (pixel-to-pixel) and spectral (frame-to-frame) analysis, was applied.

Since FP systems have multiple optical surfaces, some defocalised ghost reflections can be present (Bland-Hawthorn 1995), especially since the etalon was not tilted. To get rid of these reflections we composed a "ghost image" by using the ghost reflection of a bright star in the field (Figure 6) and numerically simulating a similar but scaled reflection for every pixel in the field. This image was then subtracted from the original. This procedure removes very efficiently all the reflected continuum and adequately but not perfectly ( $\sim 80\%$ ) the monochromatic emission.

The presence of strong night sky lines combined with photometric variations (transparency, seeing) from one exposure to another led us to proceed to a first background subtraction on each of the 27 non-redundant frames (now assembled in a 3-D cube). This background includes continuous, diffuse light and monochromatic emission from atmospheric OH radicals and from geocoronal H $\alpha$ . All these background vary both spatially and temporally. Using the radial symmetry of the FP, the sky was evaluated by azimuthally summing rings of constant phase where the galaxy signal had been masked. The computed background was then removed in each ring.

A neon calibration lamp ( $\lambda 6598.95 \text{ \AA}$ ) was used to fix the zero point at each pixel. To be totally device independent, the theoretical position of a sky emission line was then used to fine-tuned the phase (wavelength origin) at each pixel in order to get a particular wavelength on an exact x-y plane. Due to limited free spectral range, this telluric line is a

composite of geocoronal H $\alpha$  ( $\lambda 6562.74$  or  $517 \text{ km s}^{-1}$ ) and an OH line ( $\lambda 6568.78$  or  $532 \text{ km s}^{-1}$ ). Since there is no way to determine the relative contribution of each line, we are left with some uncertainties on the systemic velocity of the galaxy, but this does not affect the relative velocities and the rotation curve.

In order to get sufficient signal-to-noise throughout the image, two different Gaussian smoothings ( $\sigma=2.5$  and  $3.5$  pixels) were performed on the cube using the ADHOC package (Boulesteix 1993). Velocity maps were then obtained using the intensity weighted means of the H $\alpha$  peaks to determine the radial velocity for each pixel. A final variable resolution velocity map was constructed (Figure 7) using higher resolution for regions with originally higher signal-to-noise.

#### 4. HII KINEMATICS & OPTICAL ROTATION CURVE

The rotation curve has been obtained from the velocity field following two different methods. The first estimate was made using the task ROCUR (Begeman 1987, Coté et al. 1991) in the AIPS package, where annuli in the plane of the galaxy (ellipses in the plane of sky) are fitted to the velocity field, minimizing the dispersion inside each ring. In this way, the center, systemic velocity, position angle and inclination are evaluated. Secondly, the ADHOC package was used to fine-tune these parameters by direct visualization and comparison with a residual velocity field. The optical rotation curve at  $5''$  resolution is given in Table 4 and Figure 8. Note that there are two common ways to represent the errors on a rotation curve: the error on the mean ( $\sigma/\sqrt{N}$ ) and the velocity difference of the receding and approaching side weighted by the number of points on each side, a method often used for HI rotation curve. To be conservative, we took the maximum of the two values.

At intermediate radii, the approaching side of the galaxy is still affected by residual sky emission. This is caused by the lack of regions with pure sky signal in the most central rings, making the measurement of the sky emission lines less accurate and only partially subtracted. The final effect here is to lower the rotation velocities between  $2$  and  $4$  kpc in radius. As we will see, this is in the region where it is possible to rely with confidence on the H I data, because of the shallower fall of H I density and the slower rise of the rotation curve that make beam smearing negligible.

## 5. MASS MODELS AND PARAMETERS OF THE MASS DISTRIBUTION

The models used are described in Carignan (1985). However, instead of being “maximum disk” models, they are “best-fit” models. A  $\chi^2$  minimization technique is used in the three-parameter space of the model. Namely, those parameters are:  $(M/L_B)_*$  of the stellar disk, the core radius  $r_c$  and the one-dimensional velocity dispersion  $\sigma$  of the dark isothermal halo. Alternatively, one can use the central density  $\rho_0 = 9\sigma^2/4\pi G r_c^2$ . The surface photometry and the H I kinematics are from Côté, Carignan, & Sancisi 1991.

### 5.1. Mass Model from the H $\alpha$ Rotation Curve

The best-fit mass model for the H $\alpha$  rotation curve at 5'' resolution is shown in Fig.9. It can be seen that there is a clear sign of the disk mass in the rotation curve, which is well fitted. In fact, the best-fit model is essentially a maximum disk model. The mass-to-light ratio of the stellar disk goes from 0.3 using the H I data to 1.0 using the H $\alpha$  data, which causes the halo to become less centrally concentrated. For the dark halo, the parameters are  $r_c = 4.1$  kpc,  $\rho_0 = 0.023 M_\odot \text{pc}^{-3}$  and  $\sigma = 49.1 \text{ km s}^{-1}$ , which represent a decrease of  $\rho_0$  of more than 50%. Interestingly, the H $\alpha$  rotation curve provides a much better fit to the MOND model ( $a_0 = 1.2 \times 10^{-8} \text{ cm s}^{-2}$ ,  $M^*/L_B = 0.5$ ) than the H I curve alone (see figure 1 of Sanders 1996). However, the little kink seen at radius  $\simeq 1$  kpc could indicate the transition between the disk dominated region and the halo dominated region, which would exclude alternative gravitational theories based on luminous matter only. This feature could also be the dynamical signature of an inner bar, but the 2-D velocity field does not show evidence of non-circular motion.

It is interesting to look at the shape of the different components as a function of radius for this H $\alpha$  rotation curve, derived out to  $\sim 1.3 R_{25}$  (herein defined as  $RC3 D_{25}/2$ ) or  $\simeq 3.3' \simeq 6.0$  kpc. In massive spirals, the stellar disk usually dominates the mass distribution for  $r < R_{25}$ . Typical  $M_{dark}/M_{lum}$  are between 0.5 to 1.0 at that radius. This is certainly not the case here with  $M_{dark}/M_{lum} \simeq 4.0$  at the last measured point of the rotation curve. Moreover, at the last point, there is almost as much luminous mass in gas as in stars. So, for a dwarf spiral such as NGC 5585, the mass distribution is much more reminiscent of what is seen in dIrr (e.g. DDO 154: Carignan & Freeman 1988, Carignan & Beaulieu 1989; DDO 170: Lake, Shommer, & van Gorkom 1990) than in massive Sp galaxies ( e.g. NGC 6946: Carignan et al. 1990; NGC 3198: van Albada et al. 1985). Other late-type Sp such as IC 2574 (Martimbeau et al. 1994) and NGC 3109 (Jobin & Carignan 1990), both of type Sm, also have a strong contribution from dark matter even in the inner parts but show solid-body H I rotation curves.

### 5.2. Mass Model from the Combined H I & H $\alpha$ Rotation Curve

Table 5 gives the parameters of the mass models constructed using only the H I rotation curve, only the H $\alpha$  curve, and the combined H I & H $\alpha$  curve. For our adopted mass model of NGC 5585, we combine the high resolution of the H $\alpha$  data in the inner parts with the high sensitivity of the H I data in the outer parts. Since we are making a best-fit model, one has to understand that, because of the higher resolution, there are more H II data points than H I data points. This means that the optical data would tend to have a higher weight than the radio data. Since optical velocities are derived from high S/N data out to a radius of 120" and since Fig. 9 of Côté, Carignan & Sancisi (1991) shows that this is the region where the H I parameters are not well defined, we decided to use for the final model the H $\alpha$  data for  $r < 120''$  and the H I data for  $r > 120''$ .

This adopted model is shown in Fig.10. The parameters of the model are:  $(M/L_B)_* = 1.0$ ,  $r_c = 4.5$  kpc,  $\rho_0 = 0.024 \, M_\odot \, pc^{-3}$  and  $\sigma = 53.6 \, km \, s^{-1}$ . As expected,  $\sigma$  is very similar in the combined H I & H $\alpha$  curve as in the H I rotation curve. This is the case because this parameter is a measure of the maximum amplitude of the rotation curve, which is mainly defined by the H I data in the outer parts. However, the two other parameters  $(M/L_B)_*$  for the stellar disk and  $\rho_0$  of the dark halo (which are coupled) have nearly the same values as those derived with the H $\alpha$  curve. Again, this is because  $(M/L_B)_*$  of the luminous stellar disk, and hence the scaling parameter of the dark halo  $r_c$ , is mainly constrained by the H II data in the inner parts. Interestingly, because this newly derived central density is significantly lower, this means that this late-type galaxy's dark halo is even less concentrated; therefore this exacerbates the discrepancy between observed rotation curves and those predicted by standard CDM halo simulations, which are already too concentrated for late-type and dwarf galaxies (see, e.g., Navarro 1996 but also Kravtsov et al. 1998).

## 6. SUMMARY AND CONCLUSIONS

The importance of an accurate determination of the rising part of a rotation curve using full 2-D high resolution FP observations is well illustrated by the example of NGC 5585. The principal conclusions follow.

1. The parameters of the mass distribution of both the dark and the luminous components are very sensitive to the rising part of the rotation curve (the first few velocity points) not only in early-type spirals, where the velocity gradient is large in the inner parts, but also in late-type spirals, which have a much shallower gradient. The sensitivity is

especially important when the contributions of dark and luminous matter are comparable.

2. With the example of NGC 3198, it is shown that it is very difficult to correct theoretically for the beam-smearing effect seen in radio data.

3. Full 3-D spectroscopy, obtained with Fabry-Perot spectroscopy, is to be preferred to long-slit spectroscopy in order to derive properly the orientation parameters (namely, the rotation center and the position angle) and hence not underestimate the rotational velocities.

4. Combining new H $\alpha$  CFHT FP data with Westerbork HI data reduced the ratio  $\mathcal{M}_{dark}/\mathcal{M}_{lum}$  by  $\simeq 30\%$  via a decrease of the central density by nearly a factor of 3 for the late-type spiral NGC 5585. If such large errors are common, one could imagine that it could mask any physical correlation between the parameters of the dark and the luminous matter.

5. Finally, the optimal rotation curve is clearly a combination of 2-D high resolution spectroscopy for the inner part of spiral galaxies and high sensitivity radio observations for the outer regions.

We would like to thank the staff of the CFHT for their support during the FP data acquisition and Daniel Durand from DAO who helped with data acquisition. We also warmly thank Jacques Boulesteix for fuitfull discussion on Fabry-Perot reduction and Anthony F.J. Moffat for useful comments. CC acknowledges grants from NSERC (Canada) and FCAR (Québec).

Table 1. Parameters of the mass models of NGC 3198.

| Parameter   | H I <sup>a</sup> RC                         | Combined H I <sup>a</sup> & H $\alpha$ RC | H I <sup>b</sup> RC  |
|---|---|---|----------------------|
| <i>Luminous disk component:</i>                                 |   |   |                      |
| $(\mathcal{M}/L_B)_*$   | $(\mathcal{M}_\odot/L_\odot)$ $9.4 \pm 0.2$ | $8.5 \pm 0.3$                             | $2.8 \pm 0.5$        |
| $\mathcal{M}_*$   | $(\mathcal{M}_\odot)$ $3.2 \times 10^{10}$  | $2.9 \times 10^{10}$                      | $9.6 \times 10^9$    |
| $\mathcal{M}_{HI+He}$   | $(\mathcal{M}_\odot)$ $6.5 \times 10^9$     | $6.5 \times 10^9$                         | $6.5 \times 10^9$    |
| <i>Dark halo component:</i>                                     |   |   |                      |
| $r_c$   | (kpc) $17.2 \pm 1.0$                        | $11.7 \pm 1.0$                            | $3.9 \pm 0.1$        |
| $\sigma$  | ( $\text{km s}^{-1}$ ) $85.6 \pm 2.0$       | $79.0 \pm 1.5$                            | $83.4 \pm 1.0$       |
| $\rho_0$  | $(\mathcal{M}_\odot \text{pc}^{-3})$ 0.004  | 0.008                                     | 0.076                |
| <i>At <math>R_{HO}</math> <math>r \simeq 13</math> kpc:</i>     |   |   |                      |
| $\rho_{halo}$   | $(\mathcal{M}_\odot \text{pc}^{-3})$ 0.002  | 0.002                                     | 0.002                |
| $\mathcal{M}_{dark+lum}$  | $(\mathcal{M}_\odot)$ $6.2 \times 10^{10}$  | $6.6 \times 10^{10}$                      | $6.6 \times 10^{10}$ |
| $(\mathcal{M}/L_B)_{dyn}$                                       | 18  | 19  | 19.5                 |
| $\mathcal{M}_{dark}/\mathcal{M}_{lum}$                          | 0.76  | 1.1                                       | 4.3                  |
| <i>At the last measured point <math>r \simeq 29</math> kpc:</i> |   |   |                      |
| $\rho_{halo}$   | $(\mathcal{M}_\odot \text{pc}^{-3})$ 0.0005 | 0.0004                                    |                      |
| $\mathcal{M}_{dark+lum}$  | $(\mathcal{M}_\odot)$ $1.5 \times 10^{11}$  | $1.4 \times 10^{11}$                      |                      |
| $(\mathcal{M}/L_B)_{dyn}$                                       | 44  | 41  |                      |
| $\mathcal{M}_{dark}/\mathcal{M}_{lum}$                          | 2.9   | 3.0                                       |                      |

<sup>a</sup>Begeman 1989

<sup>b</sup>Bosma 1981

Table 2. Optical parameters of NGC 5585.

|  |   |
|--|---|
| Morphological Type <sup>a</sup>                            | SABd  |
| RA (J2000.0)   | 14 <sup>h</sup> 19 <sup>m</sup> 48 <sup>s</sup> 1 |
| Dec (J2000.0)  | 56°43'44"   |
| l  | 214 °95   |
| b  | 56 °73  |
| Adopted distance (Mpc) <sup>b</sup>                        | 6.2<br>(1' $\simeq$ 1.8 kpc)                      |
| Mean axis ratio, $q = b/a^c$                               | 0.61 $\pm$ 0.01                                   |
| Inclination( $q_0 = 0.12$ ), $i^c$                         | 53 ° $\pm$ 1 °                                    |
| Isophotal major diameter, $D_{25}^c$                       | 5.27 '  |
| Major axis PA <sup>c</sup>                                 | 99 ° $\pm$ 1°                                     |
| Exponential scale length (kpc) <sup>c</sup>                | 1.4   |
| Holmberg radius, $R_{HO}^c$                                | 3.62 '  |
| Absolute magnitude, $M_B^c$                                | -17.5   |
| Total luminosity, $L_B$                                    | $1.5 \times 10^9 L_\odot$                         |
| Helio. radial velocity ( km s <sup>-1</sup> ) <sup>a</sup> | 305 $\pm$ 3                                       |

<sup>a</sup>de Vaucouleurs et al. (1991).<sup>b</sup> $H_0 = 75$  km s<sup>-1</sup> Mpc<sup>-1</sup>.<sup>c</sup>Côté, Carignan, & Sancisi (1991).

Table 3. Parameters of the Fabry–Perot observations.

|                           |   |                                  |
|---------------------------|---|----------------------------------|
| Date of observations      |   | February 20, 1994                |
| Telescope                 |   | 3.6 m CFHT                       |
| Instrumentation:          |   |                                  |
| Focal plane instrument    |   | MOSFP                            |
| CCD detector              | 2048 $\times$ 2048 Loral3,                            | $\sigma = 8 \text{ e}^{-1}$      |
| Filter                    | $\lambda_0 = 6570 \text{ \AA}$ ,                      | $\Delta\lambda = 10 \text{ \AA}$ |
| Fabry–Perot etalon        | Scanning  | QW1162 (CFHT1)                   |
| Interference order        | $1155 @ \lambda_{\text{NEON}}$                        |                                  |
| Mean Finesse in the field | 12  |                                  |
| Calibration lamp          | Neon ( $\lambda = 6598.95 \text{ \AA}$ )              |                                  |
| Duration                  |   |                                  |
| Per channel               | 8 min/channel   |                                  |
| Total                     | 3 h 45 min  |                                  |
| Spatial Parameters:       |   |                                  |
| Field size                | $8.5' \times 8.5'$                                    |                                  |
| Pixel scale               | $0.34'' \text{ pix}^{-1}$                             |                                  |
| Spectral Parameters:      |   |                                  |
| Number of channels        | 27  |                                  |
| Free spectral range       | $5.66 \text{ \AA}$ ( $258 \text{ km s}^{-1}$ )        |                                  |
| Sampling                  | $0.2 \text{ \AA}$ ( $9.2 \text{ km s}^{-1}$ )/channel |                                  |

Table 4. Optical rotation curve at 5'' resolution<sup>1</sup>

| Radius<br>(arcsec) | $N_{app}$ | $V_{app}$<br>km s <sup>-1</sup> | $N_{rec}$ | $V_{rec}$<br>km s <sup>-1</sup> | $V_c$<br>km s <sup>-1</sup> |
|--------------------|-----------|---------------------------------|-----------|---------------------------------|-----------------------------|
| 2.5                | 27        | 10 ± 2                          | 20        | 9 ± 2                           | 11 ± 2                      |
| 7.5                | 70        | 26 ± 1                          | 59        | 25 ± 2                          | 26 ± 1                      |
| 12.5               | 104       | 33 ± 1                          | 100       | 34 ± 1                          | 33 ± 1                      |
| 17.5               | 160       | 31 ± 1                          | 99        | 33 ± 1                          | 32 ± 1                      |
| 22.5               | 198       | 33 ± 1                          | 86        | 34 ± 1                          | 33 ± 1                      |
| 27.5               | 201       | 36 ± 1                          | 100       | 32 ± 1                          | 35 ± 2                      |
| 32.5               | 195       | 40 ± 1                          | 137       | 34 ± 1                          | 37 ± 3                      |
| 37.5               | 217       | 44 ± 1                          | 173       | 38 ± 1                          | 41 ± 3                      |
| 42.5               | 211       | 44 ± 1                          | 131       | 41 ± 1                          | 43 ± 2                      |
| 47.5               | 206       | 43 ± 1                          | 125       | 46 ± 1                          | 44 ± 1                      |
| 52.5               | 194       | 46 ± 1                          | 93        | 46 ± 1                          | 46 ± 1                      |
| 57.5               | 178       | 47 ± 1                          | 103       | 45 ± 1                          | 46 ± 1                      |
| 62.5               | 193       | 46 ± 1                          | 91        | 48 ± 1                          | 46 ± 1                      |
| 67.5               | 225       | 51 ± 1                          | 54        | 45 ± 2                          | 50 ± 3                      |
| 72.5               | 270       | 57 ± 1                          | 62        | 54 ± 2                          | 56 ± 1                      |
| 77.5               | 267       | 57 ± 1                          | 72        | 53 ± 2                          | 56 ± 2                      |
| 82.5               | 285       | 61 ± 1                          | 29        | 62 ± 2                          | 61 ± 2                      |
| 87.5               | 265       | 64 ± 1                          | 6         | 43 ± 8                          | 64 ± 6                      |
| 92.5               | 288       | 66 ± 1                          | 18        | 60 ± 4                          | 66 ± 2                      |
| 97.5               | 196       | 68 ± 1                          | 70        | 62 ± 2                          | 66 ± 3                      |
| 102.5              | 86        | 71 ± 1                          | 36        | 51 ± 4                          | 67 ± 9                      |
| 107.5              | 131       | 73 ± 1                          | 17        | 55 ± 7                          | 72 ± 7                      |
| 112.5              | 105       | 72 ± 1                          | 4         | 60 ± 2                          | 72 ± 5                      |
| 117.5              | 89        | 72 ± 1                          | 37        | 61 ± 2                          | 69 ± 5                      |
| 122.5              | 86        | 74 ± 1                          | 38        | 68 ± 3                          | 73 ± 3                      |
| 127.5              | 121       | 76 ± 1                          | 48        | 59 ± 3                          | 73 ± 8                      |
| 132.5              | 179       | 73 ± 1                          | 52        | 61 ± 1                          | 70 ± 5                      |
| 137.5              | 170       | 88 ± 1                          | 62        | 65 ± 1                          | 82 ± 1                      |
| 142.5              | 160       | 87 ± 1                          | 27        | 79 ± 1                          | 86 ± 4                      |
| 147.5              | 124       | 82 ± 1                          | 56        | 77 ± 1                          | 80 ± 2                      |
| 152.5              | 72        | 84 ± 1                          | 27        | 75 ± 2                          | 81 ± 4                      |
| 157.5              | 24        | 85 ± 1                          | 113       | 76 ± 1                          | 77 ± 4                      |
| 162.5              | 44        | 82 ± 1                          | 80        | 77 ± 1                          | 79 ± 2                      |
| 167.5              | 29        | 83 ± 1                          | 35        | 79 ± 2                          | 81 ± 2                      |

Table 4—Continued

| Radius<br>(arcsec) | $N_{app}$ | $V_{app}$<br>$\text{km s}^{-1}$ | $N_{rec}$ | $V_{rec}$<br>$\text{km s}^{-1}$ | $V_c$<br>$\text{km s}^{-1}$ |
|--------------------|-----------|---------------------------------|-----------|---------------------------------|-----------------------------|
| 172.5              | 1         | $86 \pm 1$                      | 17        | $87 \pm 2$                      | $87 \pm 2$                  |
| 177.5              | 5         | $78 \pm 5$                      | 67        | $77 \pm 2$                      | $77 \pm 2$                  |
| 182.5              | 12        | $90 \pm 6$                      | 19        | $77 \pm 3$                      | $82 \pm 7$                  |
| 187.5              | 1         | $88 \pm 1$                      | 20        | $79 \pm 2$                      | $80 \pm 5$                  |
| 192.5              | 0         |                                 | 30        | $80 \pm 2$                      | $80 \pm 2$                  |
| 197.5              | 0         |                                 | 13        | $73 \pm 4$                      | $73 \pm 4$                  |

<sup>1</sup>derived with  $i = 52^\circ$ ,  $\text{PA} = 43^\circ$

Table 5. Parameters of the mass models of NGC 5585.

| Parameter   | H I RC                                  | H $\alpha$ RC        | Combined H I & H $\alpha$ RC |
|---|---|----------------------|------------------------------|
| <i>Luminous disk component:</i>                             |   |                      |                              |
| $(\mathcal{M}/\mathcal{L}_B)_\star$                         | $(\mathcal{M}_\odot/\mathcal{L}_\odot)$ | $0.3 \pm 0.3^a$      | $1.0 \pm 0.1$                |
| $\mathcal{M}_\star$   | $(\mathcal{M}_\odot)$                   | $3.3 \times 10^8$    | $9.9 \times 10^8$            |
| $\mathcal{M}_{HI+He}$                                       | $(\mathcal{M}_\odot)$                   | $1.4 \times 10^9$    | $1.4 \times 10^9$            |
| <i>Dark halo component:</i>                                 |   |                      |                              |
| $r_c$   | (kpc)                                   | $2.8 \pm 0.3$        | $4.1 \pm 0.4$                |
| $\sigma$  | ( $\text{km s}^{-1}$ )                  | $52.9 \pm 2.0$       | $49.1 \pm 2.0$               |
| $\rho_0$  | $(\mathcal{M}_\odot \text{ pc}^{-3})$   | 0.060                | 0.023                        |
| <i>At <math>R_{HO}</math> <math>r = 6.5</math> kpc:</i>     |   |                      |                              |
| $\rho_{halo}$   | $(\mathcal{M}_\odot \text{ pc}^{-3})$   | 0.0035               | 0.0041                       |
| $\mathcal{M}_{dark+lum}$                                    | $(\mathcal{M}_\odot)$                   | $1.2 \times 10^{10}$ | $1.1 \times 10^{10}$         |
| $(\mathcal{M}/\mathcal{L}_B)_{dyn}$                         |   | 10.6                 | 10.1                         |
| $\mathcal{M}_{dark}/\mathcal{M}_{lum}$                      |   | 8.7                  | 4.6                          |
| <i>At the last measured point <math>r = 9.6</math> kpc:</i> |   |                      |                              |
| $\rho_{halo}$   | $(\mathcal{M}_\odot \text{ pc}^{-3})$   | 0.0013               | 0.0017                       |
| $\mathcal{M}_{dark+lum}$                                    | $(\mathcal{M}_\odot)$                   | $1.7 \times 10^{10}$ | $1.8 \times 10^{10}$         |
| $(\mathcal{M}/\mathcal{L}_B)_{dyn}$                         |   | 15.7                 | 16.4                         |
| $\mathcal{M}_{dark}/\mathcal{M}_{lum}$                      |   | 9.5                  | 6.6                          |

<sup>a</sup>The difference in  $(\mathcal{M}/\mathcal{L}_B)_\star$  between this paper and Côté, Carignan, & Sancisi (1991) comes from using a different Galactic extinction value,  $A_B = 0.0$  (RC3).

## REFERENCES

Amram, P., Le Coarer, E., Marcelin, M., Balkowski, C., Sullivan, W.T., & Cayatte, V. 1992, A&AS, 94, 175

Amram, P., Marcelin, M., Balkowski, C., Cayatte, V., Sullivan, W.T., & Le Coarer, E. 1994, A&AS, 103, 5

Amram, P., Boulesteix, J., Marcelin, M., Balkowski, C., Cayatte, V., Sullivan, W.T. 1995, A&AS, 113, 35

Amram, P., Balkowski, C., Boulesteix, J., Cayatte, V., Marcelin, M., & Sullivan, W.T. 1996, A&A, 310, 737

Ashman, K. 1992, PASP, 104, 1109

Begeman, K.G. 1987, PhD thesis, Rijksuniversiteit, Groningen

Begeman, K.G. 1989, A&A, 225, 47

Bland-Hawthorn, J., ASP conf series, 71, 81

Bosma, A. 1981, AJ, 86, 1791

Broeils, A. 1992, PhD thesis, Rijksuniversiteit, Groningen

Boulesteix J., 1993, "ADHOC reference manual", Publications de l'Observatoire de Marseille

Carignan, C. 1985, ApJ, 299, 59

Carignan, C., & Beaulieu, S. 1989, ApJ, 347, 760

Carignan, C., Charbonneau, P., Boulanger, F., & Viallefond, F. 1990, A&A, 234, 43

Carignan, C., & Freeman, K. C. 1985, ApJ, 294, 494

Carignan, C., & Freeman, K.C. 1988, ApJ, 332, L33

Casertano, S. 1983, MNRAS, 203, 735

Corradi, R.L.M., Boulesteix, J., Bosma, A., Capaccioli, M., Amram, P., & Marcelin, M. 1991, A&A, 244, 27

Côté, S. 1995, PhD thesis, Australian National University, Canberra

Côté, S., Carignan, C., & Sancisi, R. 1991, AJ, 102, 904

Jobin, M. & Carignan, C. 1990, AJ, 100, 648

de Vaucouleurs, G., de Vaucouleurs, A., Corwin, H.G. Jr, Buta, R.J., Paturel, G., & Fouqué, P. 1991, Third Reference Catalog of Bright Galaxies (Springer-Verlag).

Kravtsov, A., & Klypin, A., Bullock, J.S. & Primack, J.R. 1998, ApJ, 502, 48

Lake, G., & Feinswog, L. 1989, AJ, 98, 166

Lake, G., Shommer, R.A., & van Gorkom, J. 1990, AJ, 99, 547

Martimbeau, N., Carignan, C., & Roy, J.-R. 1994, AJ, 107, 543

McGaugh, S.S., de Blok, W.J.G 1998, ApJ, 499, 66

Milgrom, M. 1983, ApJ, 270, 365

Navarro, J.F. 1996, ASP conf 117, eds. M. Persic & P. Salucci, 404

Sancisi, R., & Allen, R.J. 1979, A&A, 74, 73

Sanders, R.H. 1996, ApJ, 473, 117

Sicotte, V., Carignan, C., & Durand, D. 1996, AJ, 112, 1423

Swaters, R. 1999, Proceedings of Galaxy Dynamics, ed. D. R. Merritt, M. Valluri, and J. A. Sellwood, *in press*

van Albada, T.S., Bahcall, J.N., Begeman, K., & Sancisi, R. 1985, ApJ, 295, 305

Warner, P. 1973, MNRAS, 163, 163

Whitmore, B.C., Forbes, D.A., & Rubin, V.C. 1988, ApJ, 333, 542

Fig. 1.— **a)** Best fit mass model for NGC 5585 using the H I rotation curve. The model parameters are:  $(\mathcal{M}/L_B)_\star = 0.3$ ,  $r_c = 2.8$  kpc and  $\sigma = 53$   $\text{km s}^{-1}$ .

**b)** Dark-to-luminous mass ratio as a function of radius.

Fig. 2.— **a)** Maximum disk mass model for NGC 5585, where the first two points of the H I rotation curve have been given zero weight. The model parameters are:  $(\mathcal{M}/L_B)_\star = 1.0$ ,  $r_c = 3.5$  kpc and  $\sigma = 52$   $\text{km s}^{-1}$ .

**b)** Dark-to-luminous mass ratio as a function of radius.

Fig. 3.— Best fit mass model for NGC 3198 using the H I rotation curve (Begeman 1989), corrected for beam-smearing. The model parameters are:  $(\mathcal{M}/L_B)_\star = 9.4$ ,  $r_c = 17.2$  kpc and  $\sigma = 85.6$   $\text{km s}^{-1}$ .

Fig. 4.— Best fit mass model for NGC 3198 using the H I (filled circles) rotation curve (Begeman 1989) and the H $\alpha$  (open circles) rotation curve (Corradi et al. 1991). The model parameters are:  $(\mathcal{M}/L_B)_\star = 8.5$ ,  $r_c = 11.7$  kpc and  $\sigma = 79.0$   $\text{km s}^{-1}$ .

Fig. 5.— Best fit mass model for NGC 3198 using the H I rotation curve of Bosma (1981), not corrected for beam-smearing. The model parameters are:  $(\mathcal{M}/L_B)_\star = 2.8$ ,  $r_c = 3.9$  kpc and  $\sigma = 83.4$   $\text{km s}^{-1}$ .

Fig. 6.— **a)** Real reflection of a star. **b)** Cut along the y axis of the real reflection. **c)** Cut along the y axis of the simulated reflection.

Fig. 7.— Velocity field superposed on H $\alpha$  monochromatic flux.

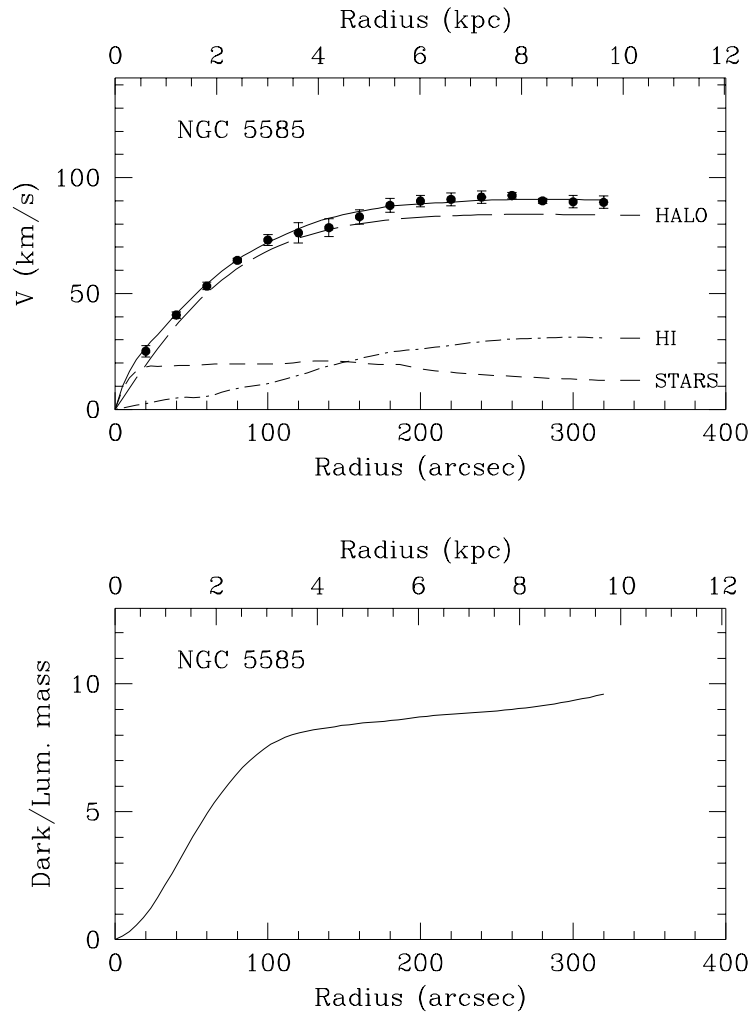
Fig. 8.— **a)** Optical rotation curve of NGC 5585.

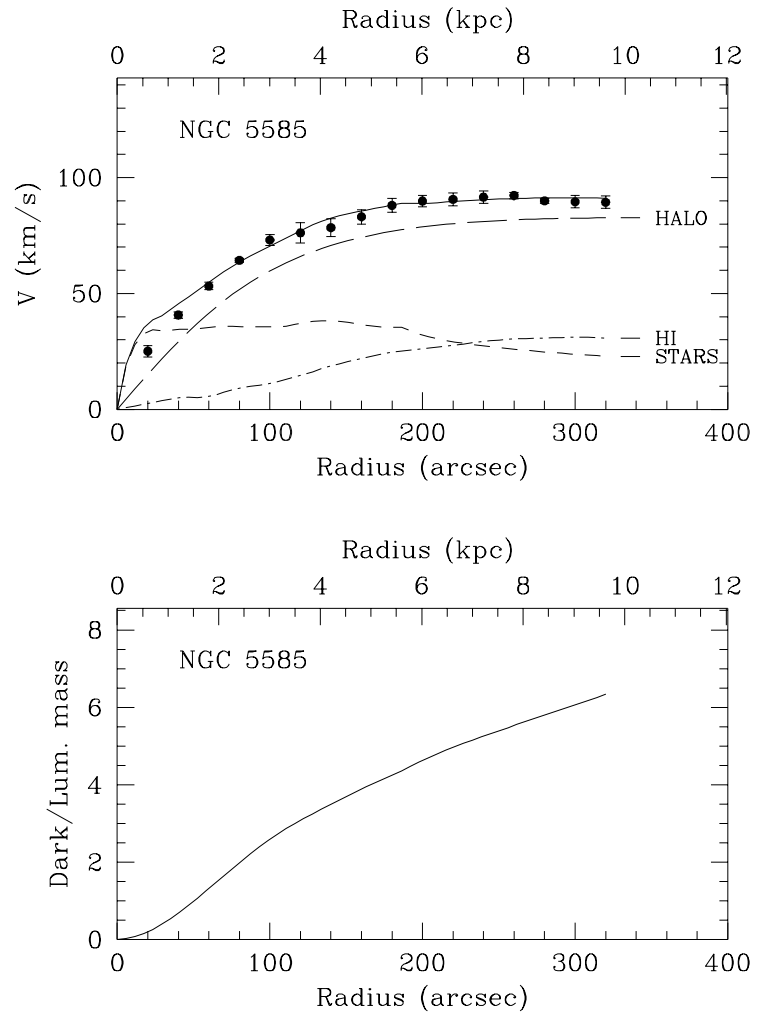
Fig. 9.— **a)** Best fit mass model for NGC 5585 using the H $\alpha$  rotation curve at 5 "resolution. The model parameters are:  $(\mathcal{M}/L_B)_\star = 0.8$ ,  $r_c = 3.7$  kpc and  $\sigma = 48$   $\text{km s}^{-1}$ .

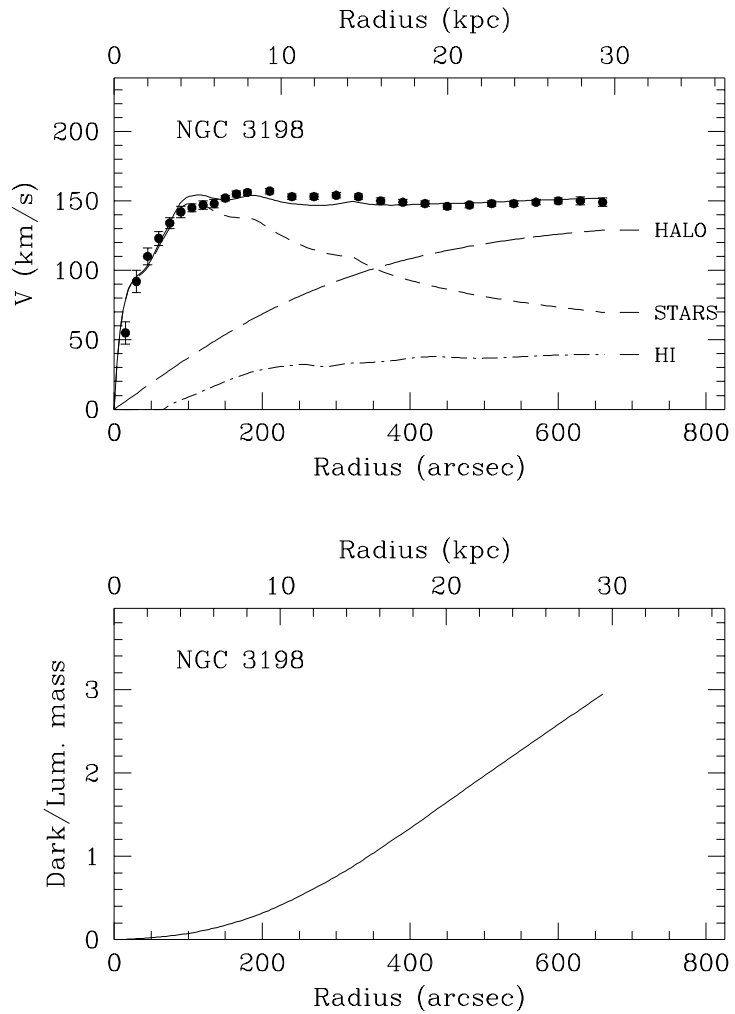
**b)** Dark-to-luminous mass ratio as a function of radius.

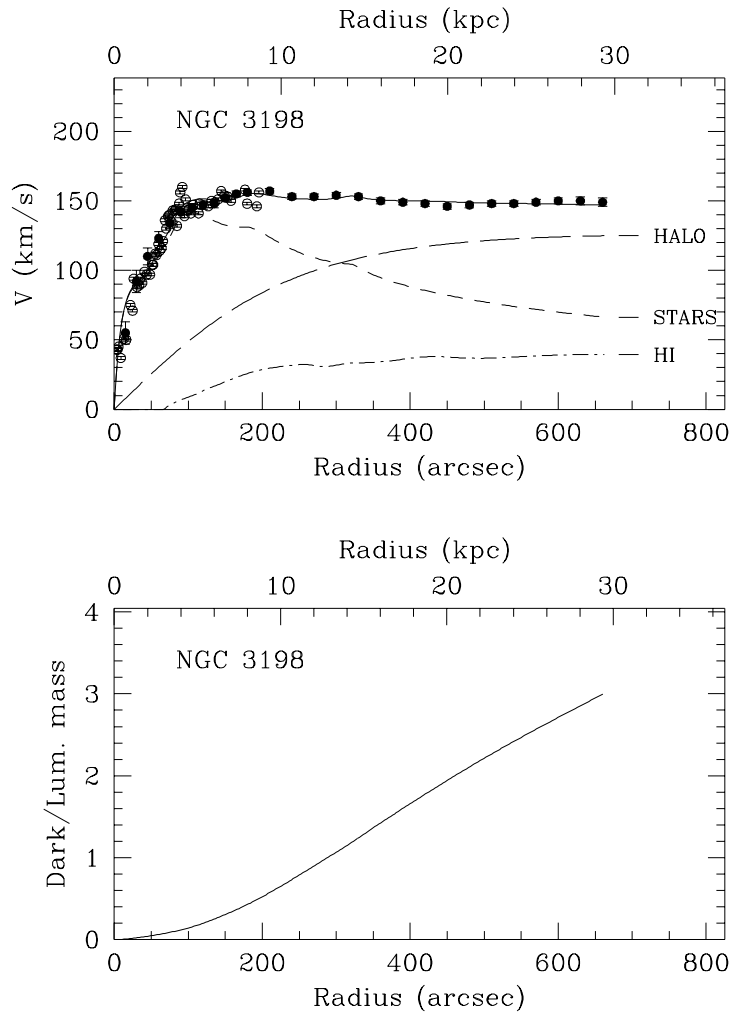
Fig. 10.— **a)** Adopted best fit mass model for NGC 5585 using the H $\alpha$  rotation curve for  $r < 120''$  and the H I rotation curve for  $r > 120''$ . The model parameters are:  $(\mathcal{M}/L_B)_\star = 0.8$ ,  $r_c = 3.9$  kpc and  $\sigma = 53.3$   $\text{km s}^{-1}$ .

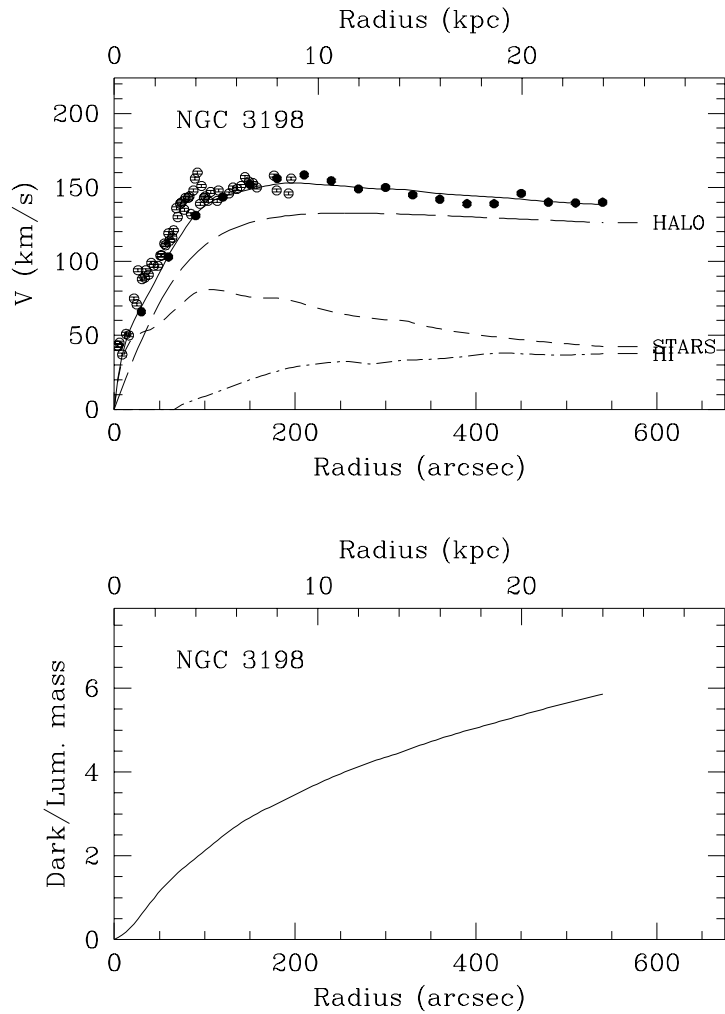
**b)** Dark-to-luminous mass ratio as a function of radius.

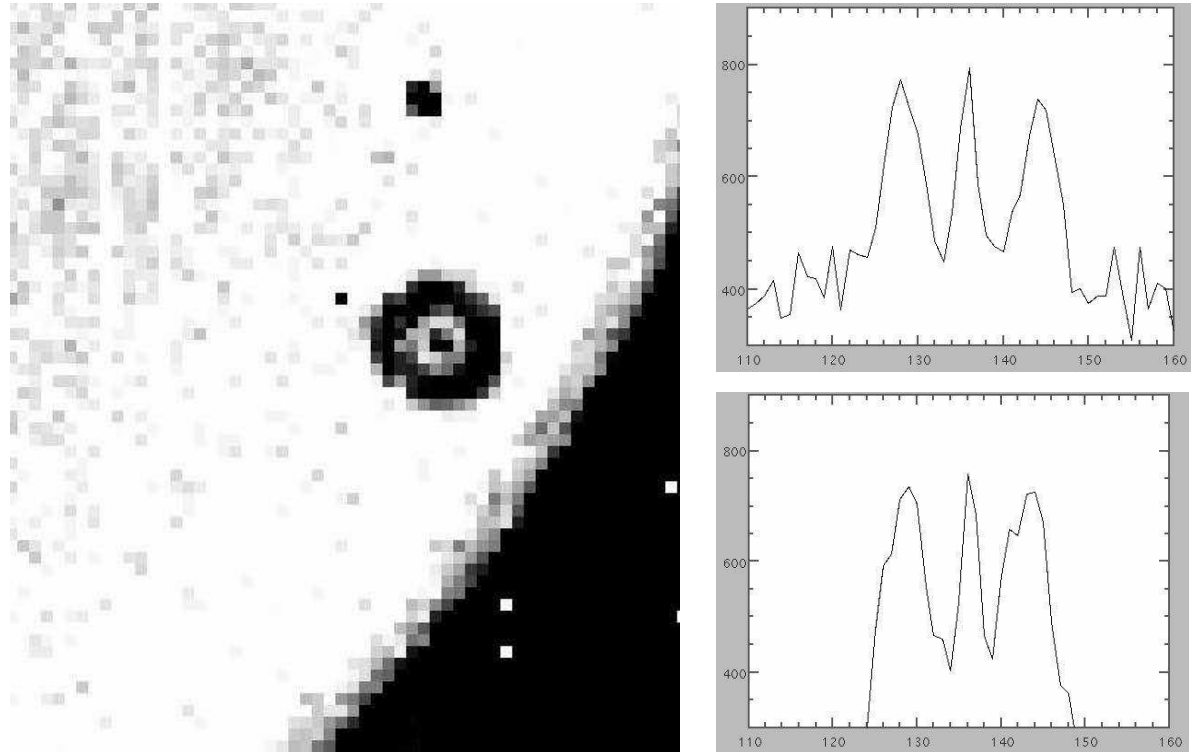


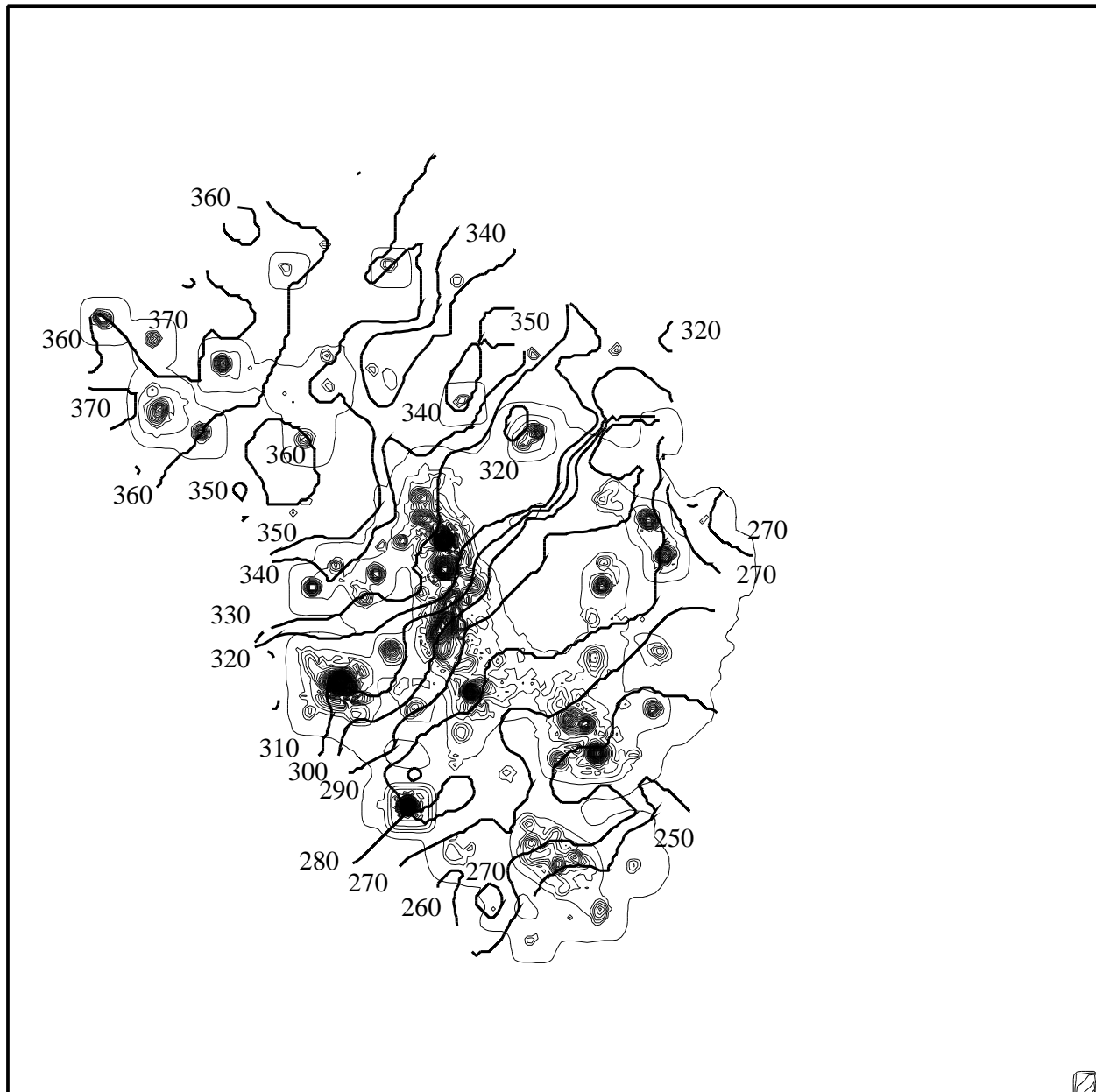












NGC 5585

